ORIGINAL ARTICLE

Excitation dynamics in Photosystem I trapped in TiO₂ mesopores

S. Szewczyk[1] · R. Białek[1] · W. Giera[1] · G. Burdziński[1] · R. van Grondelle[2] · K. Gibasiewicz[1]

Abstract

Excitation decay in closed Photosystem I (PSI) isolated from cyanobacterium *Synechocystis* sp. PCC 6803 and dissolved in a buffer solution occurs predominantly with a ~ 24-ps lifetime, as measured both by time-resolved fluorescence and transient absorption. The same PSI particles deposited in mesoporous matrix made of TiO₂ nanoparticles exhibit significantly accelerated excitation decay dominated by a ~ 6-ps component. Target analysis indicates that this acceleration is caused by ~ 50% increase of the rate constant of bulk Chls excitation quenching. As an effect of this increase, as much as ~ 70% of bulk Chls excitation is quenched before the establishment of equilibrium with the red Chls. Accelerated quenching may be caused by increased excitation trapping by the reaction center and/or quenching properties of the TiO₂ surface directly interacting with PSI Chls. Also properties of the PSI red Chls are affected by the deposition in the TiO₂ matrix: they become deeper traps due to an increase of their number and their oscillator strength is significantly reduced. These effects should be taken into account when constructing solar cells' photoelectrodes composed of PSI and artificial matrices.

Introduction

The essential features of any light-to-electrical current converter are efficient charge separation (creation of an electron–hole pair) and a series of fast secondary electron transfer events following the act of photon absorption. The secondary electron transfer increases the distance between the initial electron and hole and prevents from a charge recombination and an energy dissipation.

Photosystem I (PSI) is a photosynthetic pigment-protein complex in cyanobacteria, algae, and plants which fulfills these requirements. It converts photons to photoelectrons with exceptionally high quantum yield exceeding 99%. Therefore it is often tested in different biohybrid systems

✉ K. Gibasiewicz
krzyszgi@amu.edu.pl

1 Faculty of Physics, Adam Mickiewicz University in Poznań, ul. Uniwersytetu Poznańskiego 2, 61-614 Poznan, Poland

2 Department of Physics and Astronomy, Vrije Universiteit, De Boelelaan 1081, 1081 HV Amsterdam, The Netherlands

including solar cells (Ciesielski et al. 2008, 2010a, b; Mukherjee and Khomami 2011; Stieger et al. 2016a, b; Gunther et al. 2013; Feifel et al. 2015; Mershin et al. 2012; Gordiichuk et al. 2014; Shah et al. 2015; Yu et al. 2015; Gizzie et al. 2015; Ocakoglu et al. 2014) with the intention of invention of particularly effective device. Unfortunately, so far the efficiency of such biohybrid devices is limited. Relatively high efficiencies of some PSI-containing photoelectrodes (of the order of 0.1–0.5%) (Mershin et al. 2012; Shah et al. 2015; Yu et al. 2015) were not proven to be based on natively operating proteins.

PSI is a multi-subunit supercomplex composed of either three cores forming trimers (in the case of cyanobacteria) or a single core equipped with additional light-harvesting complexes (LHCI; in the case of some algae and plants) which increase the light absorption capacity of the core (Fig. 1). The structure of the PSI core from all these organisms is very similar to each other (Antoshvili et al. 2018; Fromme and Grotjohan 2008). It contains 96 chlorophyll (Chl) *a* molecules engaged in light absorption (Jordan et al. 2001). Six of these Chls together with two phylloquinones and three iron–sulfur clusters form a central part of the core called reaction center (RC) and are engaged in the charge separation and electron transfer (Fig. 1c). The remaining 90 Chls
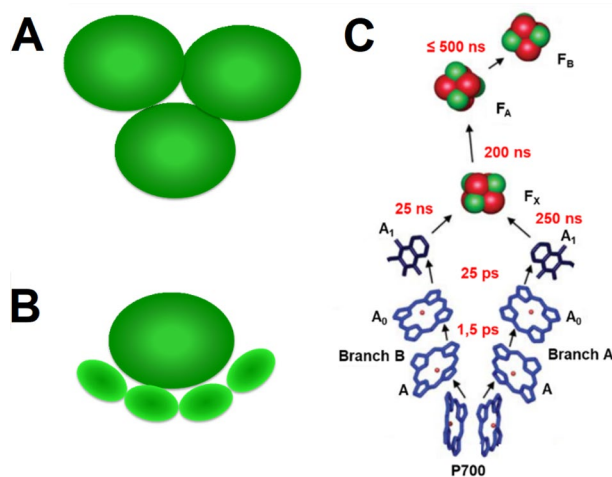
Fig. 1 Schematic presentation of trimeric PSI structure from cyanobacteria (**a**), monomeric PSI-LHCI structure from plants (**b**), and arrangement of electron transfer cofactors in PSI core with forward electron transfer lifetimes shown in red (**c**)

are called antenna Chls. Native operation of PSI has been determined over the last decades (Brettel 1997; Brettel and Leibl 2001; Nelson and Yocum 2006; Jensen et al. 2007; Holzwarth et al. 2006). It starts with a light absorption by the Chls followed by a fast excitation quenching caused by the primary charge separation between the RC molecules: primary donor (a chlorophyll a dimer labeled P700) and primary electron acceptor (either of two Chls labeled A_0) with the transient involvement of two accessory Chls (A) (Holzwarth et al. 2006; Giera et al. 2010). These three pairs of Chls together with two phylloquinones (A_1) are arranged in two quasi-symmetrical branches, both active in the electron transfer (Joliot and Joliot 1999; Guergova-Kuras et al. 2001; Li et al. 2006; Fairclough et al. 2003; Santabarbara et al. 2005, 2006; Ramesh et al. 2004, 2007; Giera et al. 2009). The two branches meet at the F_x iron–sulfur cluster, which receives an electron from A_1 and transfers it further to two terminal electron acceptors iron–sulfur clusters, F_A and F_B. The forward electron transfer events span the lifetimes from ~1 ps (primary charge separation or formation of the state $P700^+A_0^-$) to ~500 ns (formation of the state $P700^+F_B^-$) (Brettel and Leibl 2001) and are much faster than dissipative charge recombination reactions ranging from ~10 ns to ~100 ms, for the respective charge recombination reactions (Vassiliev et al. 1997; Kurashov et al. 2018) (~10 ns for $P700^+A_0^- \rightarrow P700A_0$, and ~100 ms for $P700^+F_B^- \rightarrow P700F_B$).

The primary charge separation is preceded by an excitation energy transfer from the antenna Chls to the RC that occurs with apparent/effective lifetime of 20–50 ps in PSI cores from various cyanobacteria (Gobets et al. 2001, 2003) and ~20–30 ps in PSI cores from green algae (Gibasiewicz

et al. 2001; Giera et al. 2014), and is usually longer in LHCI-containing PSI preparations from algae and plants (Giera et al. 2014; Melkozernov et al. 2004; Le Quiniou et al. 2015; Wientjes et al. 2011; Slavov et al. 2008; Abram et al. 2019) due to a relatively slow energy transfer from LHCI to PSI core. The fast, 20–50 ps, excitation quenching in the PSI core is contributed by an excitation energy transfer from the core antenna system to the RC and the primary charge separation. The primary charge separation is probably a reversible reaction and occurs many times with regeneration of the excited state in the antenna system, before the excitation is definitely quenched by formation of secondary charge separated states (Giera et al. 2010; Holzwarth et al. 2005). The primary charge separation may occur even when P700 is permanently oxidized to $P700^+$ (so called closed state of PSI) and the proposed primary charge separated state is $A^+A_0^-$, which may recombine both to the excited (Chl*) and to the ground (AA_0) state (Giera et al. 2010).

A specific feature of the PSI preparations, both cores and peripheral LHCI, is the presence of a few particularly long-wavelength Chls (called red Chls) with absorption and emission bands shifted towards the red and peaking at wavelengths longer than 700 nm (Gobets et al. 2001, 2003; Karapetyan et al. 2006; Morosinotto et al. 2003). These species originate from strong interactions between two or more Chls (Morosinotto et al. 2003; van Amerongen et al. 2000) and were hypothesized to be formed in order to (1) increase a spectral range of PSI absorption (Trissl 1993) or (2) protect PSI against an excess of light (Jensen et al. 2007; Elli et al. 2006; Carbonera et al. 2005). Their presence manifests itself in slowing down the overall excitation decay in PSI preparations (Gobets et al. 2001).

An important aspect of the application of PSI in semi-artificial devices including solar cells is the question to what extent the native mode of operation of the pigment-protein complex is preserved after its isolation from the photosynthetic membrane and its incorporation into the artificial environment. It has been demonstrated that electrodeposition of PSI cores isolated from the cyanobacterium *Synechocystis* on a flat surface of FTO glass (the glass slide covered with a thin transparent conducting layer of fluorine-doped tin oxide) resulted in a significant acceleration of the excitation decay (Szewczyk et al. 2017, 2018) and this acceleration was attributed to the dense packing of detergent-free proteins on the substrate. In the present paper we analyze how the excitation decay in PSI complexes is affected by their deposition in TiO_2 mesopores followed by evaporation of the buffer containing detergent.

Materials and methods

Isolation of PSI particles

Monomeric and trimeric forms of PSI were isolated from the wild type *Synechocystis* sp. PCC 6803 strain according to the procedure described previously (Szewczyk et al. 2017).

Preparation of TiO_2 pastes

Preparation of the TiO_2 pastes was the same as that one already described (Białek et al. 2018). For fluorescence measurements, the paste was prepared from 50-nm anatase nanoparticles (MKnano, 98% pure) with a procedure described by Woronowicz et al. (Woronowicz et al. 2012). Briefly, the paste was prepared in mortar by mixing TiO_2 nanoparticles with double-distilled water with acetylacetone followed by slow addition of double-distilled water with detergent (Triton X-100).

TiO_2 paste for pump-probe absorption measurements was prepared from P25 nanoparticles (PlasmaChem; 21 ± 5 nm) with a procedure described by Ito et al. (Ito et al. 2007) (with the exception that a three roller mill was not used). Briefly, the nanoparticles were mixed with water, acetic acid, ethanol, terpineol, and ethyl cellulose by subsequent treatments with a mortar, magnetic stirrer and ultrasonic horn (Sonics Vibra-Cell VCX130). An excess ethanol was evaporated using a rotary evaporator. This procedure was chosen for absorption measurements due to lower light scattering of the resultant layers compared to those obtained using the procedure by Woronowicz et al. (Fig. 2).

Assembly of the PSI–TiO_2 slides

Glass slides covered with FTO (Sigma-Aldrich, TEC 15) were washed in an ultrasonic bath (CT-Brand CT-432H1) sequentially in water with dish soap, double-distilled water, and ethanol for 10 min each. For fluorescence experiments,

Fig. 2 Pictures of FTO glass slides partly covered with TiO_2 layers used for fluorescence (**a**) and absorption measurements (**b**) before and after application of the PSI suspension followed by evaporation of the solvent

TiO_2 paste was then deposited on the cleaned FTO glass using a doctor-blading technique (for paste formulation see above) using Scotch 3 M Magic Tape as a mask and to define layer thickness. For the pump-probe measurements, the TiO_2 paste was deposited on the slide using a screen-printing technique with DN-HMO2 screen printer (Dyenamo) with a polyester screen of mesh count 25 (Sefar). This method gives a thinner (thus less scattering) layer than doctor-blading. This was followed by sintering in a Nabertherm 5/11 – P330 oven that was warmed up to 570 °C by 25 min and held at that temperature for the next 30 min. The active area of the TiO_2 film was ~ 0.25 cm^2 both for the fluorescence and absorption measurements (Fig. 2).

Purified PSI particles suspended in a buffer A containing 20 mM Bis–Tris (pH 7.0), 5 mM $MgCl_2$, 5 mM $CaCl_2$, 10 mM NaCl, 0.03% β-DM v/v were diluted in the same buffer to $OD_{680\,nm,\,1\,cm} = 12$. Next, 4 µl of such a suspension was placed on the TiO_2 surface and stored at 4 °C for ~ 12 h to evaporate the solvent. The PSI–TiO_2 substrates were gently rinsed by distilled water before time-resolved experiments to wash out loosely attached proteins.

Procedure of deposition of PS I on FTO glass

The procedure of deposition of PS I on the FTO glass was described in detail before (Szewczyk et al. 2017, 2018). Shortly, a drop of PSI solution with a reduced amount of salts and detergent was placed between two FTO electrodes, separated by a ~ 2 mm spacer. Next, the voltage of 2.5 V was applied for 5 min between the electrodes. After that, the sample was left for 12 h at 4 °C in order to evaporate the solvent.

Time-resolved measurements

The time-resolved fluorescence spectroscopic experiments were carried out with a streak camera setup (Laser Center, Vrije Universiteit, Amsterdam), which was described before (Szewczyk et al. 2017). The 800-nm, 100-fs laser pulses were generated in the Ti:Sapphire laser (Coherent Vitesse) and amplified by the regenerative amplifier (Coherent RegA 9000). Their second harmonic (400 nm) obtained in the optical parametric amplifier (Coherent OPA 9400) was used for the sample excitation in all experiments. Conditions of the experiments (the energy of the pulse < 1 nJ, the repetition rate of the laser pulses—125 kHz, the spot size of the laser beam on the sample— ~ 150 µm) were chosen to exclude the singlet–singlet annihilation effects. Fluorescence signal was collected by the streak camera (Hamamatsu C5680), in three different time domains: ~ 140 ps, ~ 400 ps and ~ 1400 ps. The time resolution (temporal width of the scattered laser pulses) in those modes was ~ 3.5, ~ 6 and ~ 15 ps, respectively.
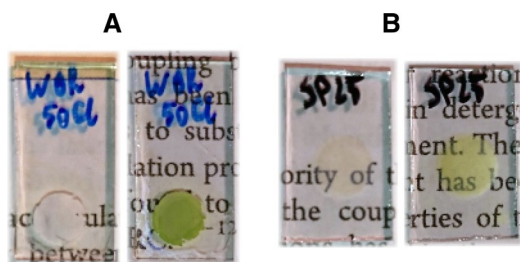
The transient absorption measurements were performed using the Helios transient absorption spectrometer (Ultrafast Systems) described earlier (Szewczyk et al. 2018). The excitation beam was generated by the Ti:Sapphire oscillator (Mai-Tai, Spectra Physics) followed by the regenerative amplifier (Spitfire Ace, Spectra Physics). The amplifier output (800 nm, 100-fs pulses) was split to generate two beams: (1) pump (405 nm) in the optical parametric amplifier (Topas Prime), and (2) probe—white-light continuum in 440–780 nm range using a sapphire crystal. The used setup enables measurements in a 2.9-ns time window with a ~ 200-fs time resolution. The energy of a single pump pulse was kept at about 15 nJ with a spot size of approximately 300 μm. Such excitation conditions minimalized singlet–singlet annihilation effects.

The PSI samples (both in solution and immobilized on TiO_2) in both types of measurements were continuously moved to minimize effects related to an excessive irradiation. In control time-resolved fluorescence experiments (PSI in solution) the PSI suspension was placed in the rotating cuvette (~ 10 cm diameter, 2-mm thickness of the solution layer) and its concentration was set to $OD_{680 \, nm, 1 \, cm} = 1$. For the rest of the experiments, the 2D mechanical motion controller (Newport) was used in order to move the samples in horizontal and vertical dimension. As a result, the laser beams scanned the sample in a Lissajous-like pattern. For the time-resolved absorption measurements of PSI in solution, samples were diluted in the buffer A to $OD_{680 \, nm, 1 \, cm} = 2$ and placed in a 2 mm thick quartz cuvette.

The measurements of PSI in solution and PSI in TiO_2 were performed without addition of any redox mediator, in order to hold similar redox conditions. Under these conditions, the PSI complexes remained in the closed state (P700 permanently oxidized to $P700^+$) as evidenced by the lack of

long lived absorption changes at 700 nm characteristic of formation of $P700^+$ (see below).

Global and target analyses of the collected data were performed using Glotaran software (Snellenburg et al. 2012).

Results and discussion

In Fig. 3, kinetics of fluorescence (panel a) and transient absorption (panel b) at 687 nm from three different systems containing closed PSI are compared: PSI trimers dissolved in a detergent-containing buffer, detergent-free PSI trimers electrodeposited on FTO, and PSI trimers deposited in mesoporous layer of TiO_2. Both techniques clearly demonstrate that the excitation decay in PSI trimers trapped in TiO_2 mesopores is significantly accelerated on a 100-ps time scale compared to the PSI trimers dissolved in a buffer. On the other hand, the effect of the accelerated decay in TiO_2 on this time scale is similar to that one observed on PSI deposited on a flat FTO-covered glass [compare also (Szewczyk et al. 2017, 2018)]. The acceleration effect is larger in fluorescence than in transient absorption because the excitation decay is followed by a transient formation of the non-emitting short-lived charge-separated state ($A^+A_0^-$) which slows down the decay of the photobleaching (panel b) but not the decay of emission (panel a).

The fluorescence decay in the PSI trimers in a solution contains a small long-lived component, not decaying to zero on the presented ~ 1.3-ns time scale (Fig. 3a). Such a component with a ~ 5-ns lifetime (see below) is commonly observed in virtually all PSI preparations and assigned to PSI Chls energetically uncoupled from the RC (Giera et al. 2010, 2014; Gobets et al. 2001, 2003; Gibasiewicz et al. 2001; Le Quiniou et al. 2015; Slavov et al. 2008; Holzwarth et al. 2005; Szewczyk et al. 2017, 2018, 2020; Savikhin
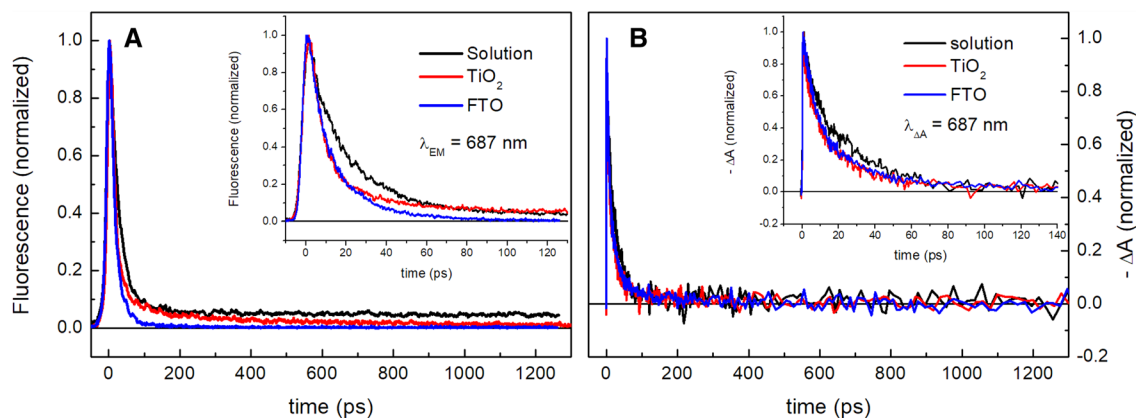

Fig. 3 Comparison of fluorescence (**a**) and transient absorption (**b**) kinetics of PSI trimers from *Synechocystis* dissolved in a buffer solution, deposited on FTO glass, or trapped in TiO_2 mesopores. Excitation was set at 400 nm. Note that the negative ΔA signal in panel b was inverted in order to facilitate comparison with fluorescence data presented in panel a

et al. 1999). Interestingly, this phase is missing in the case of PSI-FTO system [compare (Szewczyk et al. 2017)], and is replaced by an intermediate phase slowly decaying (~ 0.5 ns, see below) for the PSI–TiO$_2$ sample. The non-decaying and slowly decaying phases seen in fluorescence of PSI solution and PSI–TiO$_2$ samples (Fig. 3a) are not clearly visible in the absorption kinetics (Fig. 3b) due to a poorer signal to noise ratio. However, these phases are well resolved in the global and target analysis of the absorption data (see below).

Figure 4 presents results of global (DAS) and target (SAS) analysis of the time-resolved fluorescence measurements of closed PSI in the solution, deposited on FTO (adapted from ref. Szewczyk et al. 2017), and in the TiO$_2$ mesopores. In all the cases, the global analysis yielded two sub-100-ps components of similar spectral positions, shapes, and lifetimes (4.9 ps and 24 ps in solution, 6.9 ps and 22 ps on FTO, 6.1 ps and 41 ps in TiO$_2$) but of very much different relative amplitudes (panels a–c). In the solution, the 4.8-ps component clearly describes the energy equilibration process between bulk Chls emitting at ~ 687 nm and red shifted Chls emitting at ~ 715 nm. The larger amplitude of the positive part of this DAS than its negative part reveals a minor contribution of the overall excitation decay occurring on the same time scale. On the other hand, the 24-ps DAS peaking at ~ 687 nm is of a higher amplitude, is much broader and

asymmetric with a bump above 700 nm on a long-wavelength slope of the band, and is positive in the whole spectral range. Therefore, this DAS is assigned to the decay of the excitation equilibrated over the bulk and long-wavelength Chls. In contrast to the PSI in solution, the short, 6.1-ps DAS strongly dominates in the overall decay of excitation in the PSI–TiO$_2$ system and no negative amplitudes attributable to excitation equilibration are seen. The 41-ps DAS is broadened towards the red similarly as the 24-ps DAS for PSI in solution but is of small amplitude. Apparently, most of the excitation decays from the bulk Chls non-equilibrated with the red-shifted Chls, and only a minority of excitation is equilibrated between the bulk and red Chls and decays with 41-ps lifetime. The relative amplitude of the 22-ps DAS in the PSI-FTO system is intermediate between the corresponding DAS-es for PSI in solution and in TiO$_2$. In addition to the sub-100-ps DAS, a 5-ns DAS (peaking at ~ 679 nm) as well as a 0.5-ns DAS (peaking at ~ 670 and at ~ 700 nm) of very small amplitudes were resolved in PSI solution and PSI–TiO$_2$ systems, respectively, and are discussed below.

The features seen in the DAS are reflected in the results of target analysis (TA). The compartmental model used in TA is shown in Fig. 5 and the resultant rate constants are collected in Table 1. Three compartments were taken into account to model the fluorescence data of PSI in solution,
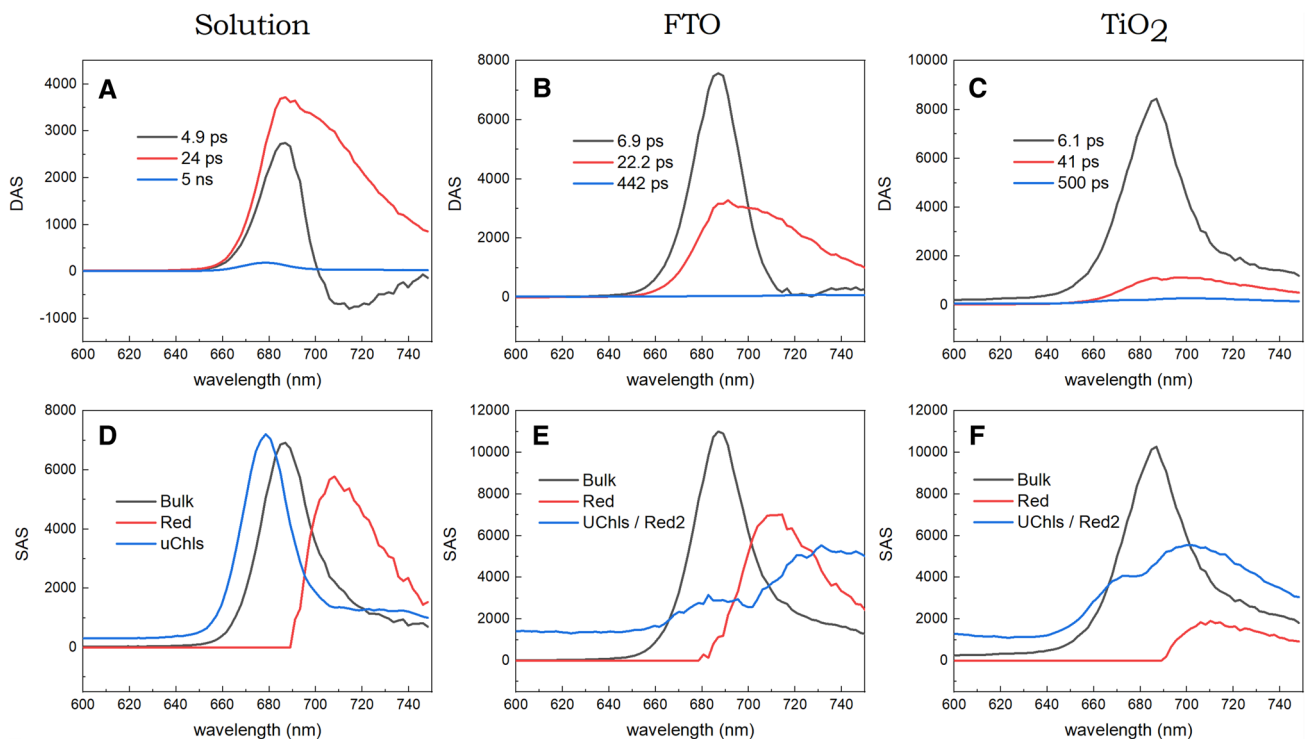

Fig. 4 Comparison of global (DAS; **a–c**) and target (SAS; **d–f**) analysis results obtained for time-resolved fluorescence data of PSI trimers from *Synechocystis* dissolved in a buffer solution (**a, d**), deposited on FTO [**b, e**, adapted from ref. (Szewczyk et al. 2017)], or trapped in TiO$_2$ mesopores (**c, f**). Excitation was set at 400 nm
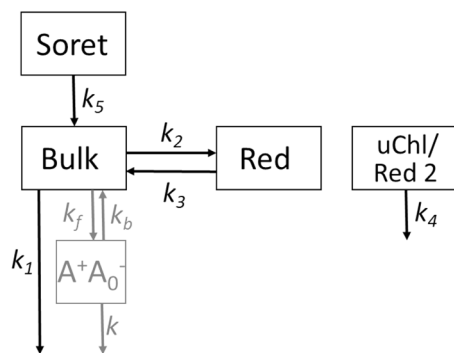
Fig. 5 In black: compartmental model used in target analysis of results of time-resolved fluorescence and time-resolved absorption shown in Figs. 4 and 6 (SAS). In gray: rate constants (k_f, k_b, and k) affecting the value of k_1; in the closed RCs, k depicts charge recombination reaction ($A^+A_0^- \rightarrow AA_0$)

PSI on FTO, and PSI in TiO$_2$: bulk Chls, red Chls being in equilibrium with bulk Chls, and uncoupled Chls (uChls) (mixed in one compartment with a second pool of red Chls in the case of PSI–TiO$_2$ system—see below). In the case of the transient absorption data, characterized by about ten times better temporal resolution than the fluorescence data, an additional compartment, "Soret", was introduced

in order to model sub-picosecond processes of (1) the relaxation from the initially excited Soret state to the Q$_y$ state and (2) the excitation relaxation between relatively high-energy (blue shifted) Chls and bulk Chls.

The spectra of the three emitting compartments resulting from TA for the PSI in solution are shown in Fig. 4d and are very similar to those published before (Szewczyk et al. 2017). A maximum of bulk Chls emission is at ~ 687 nm, a maximum of red Chls emission—at ~ 710 nm, and a maximum of the uChls—at ~ 679 nm. After introducing PSI into the TiO$_2$ mesopores (Fig. 4f), the bulk Chls compartment remains almost unaffected (except for a modest broadening), the red Chls compartment preserves its shape but its amplitude is reduced by a factor of ~ 3, and the uChls compartment is characterized by two bands—one typical for uChls (peaking at ~ 670 nm) and another one, red-shifted to ~ 700 nm. The reduced amplitude of the red Chls SAS in the TiO$_2$ mesopores may be explained by a reduced oscillator strength caused by the interaction of PSI complexes with the TiO$_2$ substrate. A similar, although significantly less pronounced effect was observed before for PSI tightly deposited on a flat surface of FTO glass (Fig. 4e). Also the double-peak structure of the similar 0.5-ns SAS was observed before for PSI on

Table 1 Parameters obtained from global and target analysis of time-resolved fluorescence and transient absorption data obtained for the closed PSI complexes from *Synechocystis* in solution, deposited on FTO, and incorporated into the TiO$_2$ mesopores

		Trimers						Monomers					
		Fluorescence			Absorption			Fluorescence			Absorption		
		Solution	FTO[a]	TiO$_2$	Solution	FTO[b]	TiO$_2$	Solution[a]	FTO[a]	TiO$_2$	Solution[b]	FTO[b]	TiO$_2$
Global analysis	τ_1 [ps]	–	–	–	0.4	0.7	0.4	–	–	–	0.6	0.6	0.3
	τ_2 [ps]	4.9	6.9	6.1	3.2	5.1	4.4	5.3	6.5	5.4	4.2	4.2	4.3
	τ_3 [ps]	24	22	41	24	24	25	24.5	24.5	29	25	22	30
	τ_4 [ps]	5 000	442	500	5 000	454	900	5 000	227	500	5 000	625	1 600
Target analysis	$1/k_1$ [ps]	15.5	10.5	10.1	17.5	14.3	14.8	16.1	10.3	9.6	20.0	13.1	16.9
	$1/k_2$ [ps]	19.6	36.7	21.1	14.4	22.0	15.6	23.3	30.0	18.5	22.3	15.4	13.6
	$1/k_3$ [ps]	7.8	14.1	25.4	4.4	7.9	7.4	8.1	15.4	16.3	5.3	7.2	7.6
	$1/k_4$ [ps]	5 000	442	500	5 000	454	900	5 000	228	500	5 000	626	1 600
	$1/k_5$ [ps]	–	–	–	0.4	0.7	0.4	–	–	–	0.3	0.6	0.3
	ΔG^0_{b-r} [meV]	− 23	− 25	+ 5	− 30	− 26	− 19	− 27	− 17	− 3	− 37	− 20	− 15
	ΔH^0_{b-r} [meV]	+ 61	+ 59	+ 61	–	–	–	+ 62	+ 52	+ 63	–	–	–
	N_r	4	4	10	–	–	–	3	6	7	–	–	–

τ_i—lifetimes obtained from global analysis; k_i—rate constants obtained from the target analysis; $\Delta G^0_{b-r} = G^0_b - G^0_r = -k_B T \ln\frac{k_3}{k_2}$ is the standard (Gibbs) free energy difference between bulk (G^0_b) and red (G^0_r) compartments in Fig. 5 (k_B—Boltzmann constant, T—absolute temperature); $\Delta H^0_{b-r} = hc(\frac{1}{\lambda_b} - \frac{1}{\lambda_r})$ is the standard enthalpy difference between bulk and red Chls states (h—Planck constant, c—speed of light in vacuum, λ_b and λ_r—respective wavelengths of the bulk and red Chls SAS at their maxima—see Fig. 4; see (Szewczyk et al. 2017, 2018) for further details). N_r—effective number of red Chls estimated on the basis of ΔG^0_{b-r} and ΔH^0_{b-r}

[a]Values taken from (Szewczyk et al. 2017)

[b]Values taken from (Szewczyk et al. 2018). In the references (Szewczyk et al. 2017, 2018), 3 mM potassium ferricyanide was added to the solution of PSI in order to keep P700 oxidized

FTO, albeit with maxima at longer wavelengths of ~680 and ~730 nm (Szewczyk et al. 2017) (Fig. 4e).

In Fig. 6, DAS and SAS obtained from an analysis of time-resolved absorption measurements are compared. For both PSI samples, the sub-picosecond DAS (Fig. 6a, b) describes a mixture of Soret to Q_y internal conversion and the blue to bulk Chls energy transfer—mixing of both processes is reflected by the non-conservative shape of the respective DAS with smaller negative part (at ~670 nm) and larger positive part (at ~690 nm). The second DAS of 3.2–4.4 ps depicts, similarly to the respective fluorescence DAS (Fig. 4a, c), mostly excitation energy transfer from bulk to red Chls in the case of PSI in solution, and mostly excitation decay in the case of PSI–TiO$_2$ sample. The difference between these two DAS reflects faster decay of photobleaching/stimulated emission signal in PSI–TiO$_2$ than in PSI in solution seen in Fig. 3b. The third DAS, of 24–25 ps lifetime, corresponds to the 24–41-ps DAS from Fig. 4a, c. The effect of introducing PSI into the TiO$_2$ mesopores on this component is similar to that observed in fluorescence (Fig. 4a, c) albeit less dramatic—the relative amplitude of this phase decreases. The smaller effect seen in absorption may be explained by contribution from the photobleaching

of the charge separated dark state $A^+A_0^-$ which is absent in the fluorescence data. The slowest DAS decays within 5 ns for PSI in solution and in 0.9 ns in PSI–TiO$_2$ and similarly as in fluorescence data is assigned to, respectively, uncoupled or weakly coupled Chls as suggested by long lifetimes and blue-shifted position of the peaks (to ~674–680 nm).

TA of the absorption data (Fig. 6c, d) reveals mostly the same features as in the case of the fluorescence data. The signal from the bulk Chls peaks in both samples at ~685 nm (slightly blue shifted, due to Stokes shift, relative to the bulk Chls emission peaking at ~687 nm). Maximum of the red Chls pool is at ~705 nm in both samples (again ~5-nm blue shifted relative to the fluorescence SAS in Fig. 4d, f). Uncoupled Chls bands peak at ~675–680 nm, towards the blue relative to the bulk Chls, as expected. In contrast to the fluorescence data (Fig. 4f) the uChls compartment in absorption (Fig. 6d) does not possess any red Chls contribution. The reason for this minor difference remains unclear.

TA of the absorption data yields also a spectrum of the "Soret" compartment. It should be interpreted as a mixture of two very similar spectra. One is a pure Q_y photobleaching spectrum of bulk Chls without significant contribution of stimulated emission (spectrum of the bulk Chls
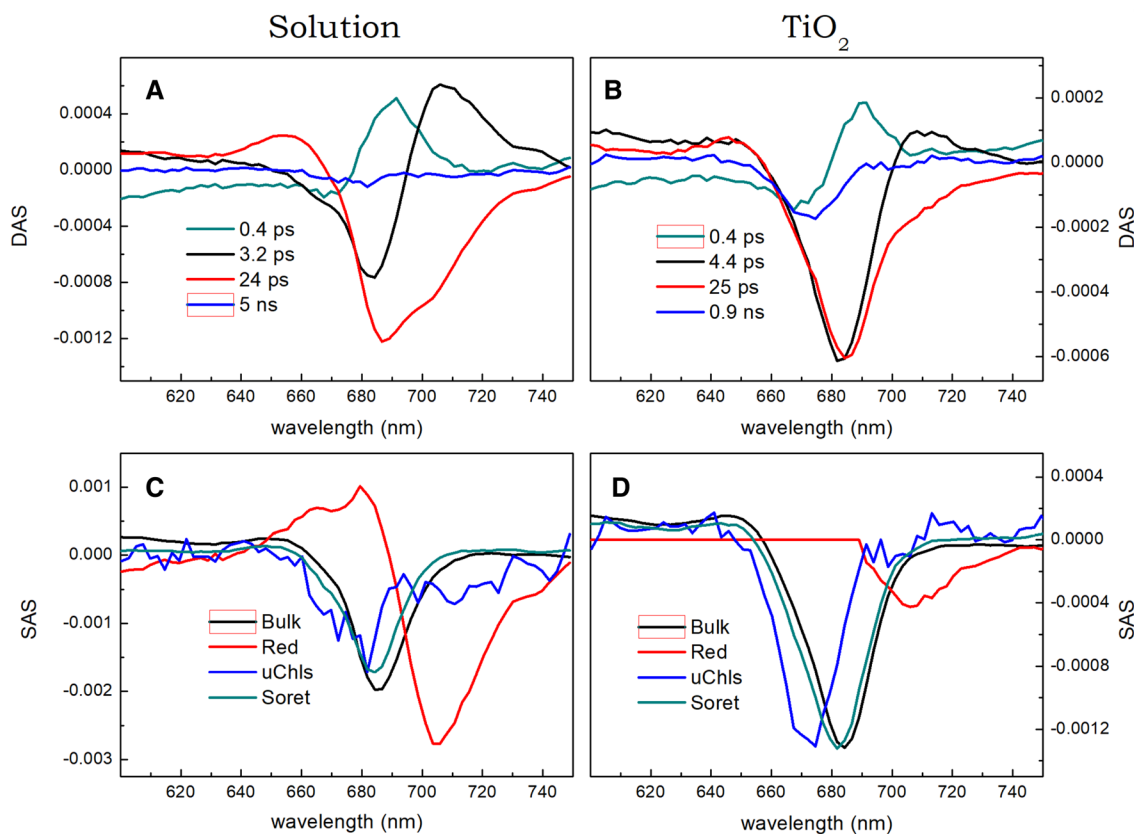

Fig. 6 Comparison of global (DAS; **a**, **b**) and target (SAS; **c**, **d**) analysis results obtained for transient absorption data of PSI trimers from *Synechocystis* either dissolved in a buffer solution (**a**, **c**) or trapped in the TiO$_2$ mesopores (**b**, **d**). Excitation was set at 400 nm

before the internal conversion from the Soret to Q_y band took place). Another one is a Q_y photobleaching spectrum of relatively blue-shifted bulk Chls with a contribution of stimulated emission (after internal conversion). In the solution (Fig. 6c), both spectra are represented and therefore the amplitude of the "Soret" spectrum is smaller than the amplitude of the "Bulk" spectrum. In TiO_2 (Fig. 6d), the "Soret" and "Bulk" spectra are of similar amplitudes and the 0.4-ps DAS (Fig. 6b) is more conservative than in solution (Fig. 6a). These features indicate that the "Soret" spectrum in Fig. 6d is dominated by the latter component—blue Chls photobleaching plus stimulated emission. In both cases (Fig. 6c, d), a similar shape of the "Soret" and "Bulk" spectra together with a slight red-shift of the latter one are understandable and expected.

The values of the reciprocals of the rate constants shown in Fig. 5, obtained from the TA are collected in Table 1 both for the trimeric and monomeric PSI complexes in the solution, on FTO, and in the TiO_2 mesopores. The values obtained for the monomeric PSI are very much consistent with those for the trimeric PSI and therefore, only the latter ones will be discussed in detail. The major observation explaining the acceleration of the fluorescence and absorption signal decay (Fig. 3) following deposition of PSI in the TiO_2 mesopores is shortening of $1/k_1$ from 15.5 to 10.1 ps in fluorescence (corresponding to ~ 50% increase of k_1) and from 17.5 to 14.8 ps in the absorption experiment. Longer lifetimes in the case of the absorption are consistent with the involvement of the state $A^+A_0^-$ (detected in the absorption but not in the fluorescence) which appears in the closed RCs and decays slightly slower than the excited state (Giera et al. 2010). Expected involvement of the dark state $A^+A_0^-$ in excitation decay and its influence on the rate k_1 is presented in Fig. 5 by the gray part of the scheme.

Acceleration of the process depicted by the rate k_1 in response to incorporation of the PSI complexes into TiO_2 is responsible for quenching of the large majority ($\sim 70\% = \frac{k_1}{k_1+k_2} 100\%$) of bulk Chls excitation before equilibration between the bulk and red Chls occurs. Similar acceleration of the bulk Chls quenching in PSI was observed before for PSI trimers and monomers deposited on silan- or FTO-covered glass and it was concluded to be caused by the dense PSI packing on the flat surface (Szewczyk et al. 2017, 2018). Such a dense packing was possible due to the removal of detergent from the PSI solution by dialysis, that in turn promoted side-side interaction between the PSI proteins. However, the solution of the PSI complexes deposited on TiO_2 contained detergent. Moreover, the mesoporous structure of TiO_2 gives enough free space for accommodation of all applied PSI proteins. For these reasons no crowding effect in the case PSI–TiO_2 system is expected. Therefore we propose that the reason for the accelerated quenching is

adhesion of PSI complex to solid substrate inducing (1) increased excitation trapping by RC and/or (2) excitation quenching by the TiO_2 surface directly interacting with the PSI Chls.

Another effect of the PSI interaction with the interior of the mesopores is significant ~ 1.5–3-fold increase in the lifetime $1/k_3$ (Table 1; Figs. 5 and 7). This effect, together with less significant modifications of the $1/k_2$ values, reveals a shift in the Bulk ↔ Red equilibrium towards the red. Apparently, the free energy of red Chls shifts down relative to bulk Chls as a result of the PSI deposition in mesopores. This is reflected by different free energy gap, ΔG^0_{b-r}, between bulk and red Chls in PSI in TiO_2 than in solution (Table 1). This shift partly counteracts the acceleration of the excitation decay caused by shortening of the lifetime $1/k_1$.

The reason why the free energy gap, ΔG^0_{b-r}, increases following the PSI deposition in TiO_2 pores, despite almost unchanged spectral position of the bulk (~ 687 nm) and red (~ 708–710 nm) Chls (compare Fig. 4d, f), may be increased number of red Chls in the PSI–TiO_2 system. As can be seen in Table 1, the free enthalpy difference between bulk and red Chls, ΔH^0_{b-r}, calculated from the peak positions of the bulk and red Chls SAS, is identical for PSI in solution and in TiO_2. On the basis of ΔG^0_{b-r} and ΔH^0_{b-r}, it is possible to estimate the number of red Chls per PSI monomer, assuming the total number of ~ 100 Chls per PSI monomer, from the following expression derived from the equations given in references (Szewczyk et al. 2017, 2018):

$$N_r = \frac{100}{1 + e^{\frac{\Delta H^0_{b-r} - \Delta G^0_{b-r}}{k_B T}}}.$$

The resulting number of red Chls per monomeric PSI deposited in TiO_2 (10 and 7 for PSI trimers and monomers, respectively) is ~ 2.5-fold larger than the number of red Chls in PSI in solution (Table 1). In consequence, the decreased oscillator strength of the red Chls (see above) is compensated by their increased number. This compensation could
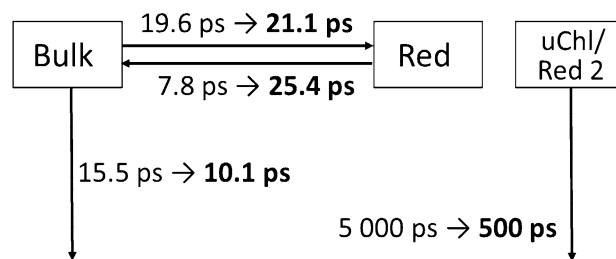
Fig. 7 Comparison of the molecular lifetimes resulting from the target analysis of the fluorescence measurements of PSI trimers in solution (regular font) and incorporated into the TiO_2 mesopores (in bold; compare Table 1). Distribution of the initial excitation was ~ 92%—Bulk, ~ 4%—Red, ~ 4% uChl/Red 2

be the reason why no significant differences between the steady-state absorption spectra of PSI in solution and in TiO_2 are observed in the long-wavelength region, > 680 nm (Fig. S1 in the Supplementary Information). A similar, two-fold increase in the number of red Chls was reported before for PSI monomers deposited on FTO (Szewczyk et al. 2017).

A separate question is what is the nature of the additional red Chls. We hypothesize that the new red states may come from groups of the PSI (peripheral?) Chls which in the solution are bulk Chls weakly interacting with each other, but forced by the interaction with the TiO_2 substrate, they become excitonically coupled systems.

Regarding the large decrease in the oscillator strength of the red Chls after the PS I deposition on TiO_2 we speculate that it may be caused by redistribution of the oscillator strength from the low-energy (long wavelength, > 700 nm) to the high-energy excitonic bands (of interacting Chls forming the red states), with the latter ones spectrally overlapping with the bulk Chls. Thus, the total oscillator strength of the excitonically interacting Chls does not need to be affected by the interaction between PSI and TiO_2. It is known that the distribution of the oscillator strength between excitonic states critically depends on the mutual orientation of the interacting molecules (van Amerongen et al. 2000). The new red states appearing as a result of the interaction between PSI and TiO_2 may come from the excitonically interacting Chls whose mutual orientation privileges high contribution of the higher excitonic state(s) at the expense of the oscillator strength of the low energy band (> 700 nm).

Finally, one should consider the potential influence of the elevated salt concentration in the vicinity of the PS I complexes immobilized in the TiO_2 pores after the evaporation of the solvent. First, the immobilized PSI particles are expected to be covered with a layer of detergent molecules protecting the proteins from the direct contact with the salt. Secondly, the slow evaporation should result in crystallization of the salt. Under such assumptions, no ions should strongly interact with the protein surface and no influence of the elevated salt concentration on the excitation dynamics in PS I trapped in the TiO_2 mesopores is expected.

Conclusions

Incorporation of the PSI cores in the TiO_2 matrix leads to three clear effects which are summarized in Fig. 7 and affects all three compartments considered in the model: bulk, red, and uncoupled Chls. (1) Excitation of bulk Chls decay is accelerated by ~ 50%. A similar acceleration was previously observed for PSI cores deposited on the FTO glass (Szewczyk et al. 2017). (2) The red Chls become deeper traps and their oscillator strength is reduced by a factor of ~ 3. (3) The lifetime of the uncoupled Chls decreases and their spectrum

becomes complex with an additional band in the red. These effects should be taken into account when constructing PSI-containing semi-artificial biohybrid materials.

Compliance with ethical standards

Conflict of interest The authors declare that they have no conflict of interest.

References

Abram M, Białek R, Szewczyk S, Karolczak J, Gibasiewicz K, Kargul J (2019) Remodeling of excitation energy transfer in extremophilic red algal PSI-LHCI complex during light adaptation. Biochim Biophys Acta. https://doi.org/10.1016/j.bbabio.2019.148093; (in press)

Antoshvili M, Caspy I, Hippler M, Nelson N (2018) Structure and function of photosystem I in *Cyanidioschyzon merolae*. Photosynth Res 139:499–508

Białek R, Swainsbury D, Wisner JK, Jones M, Gibasiewicz K (2018) Modelling of the cathodic and anodic photocurrents from *Rhodobacter sphaeroides* reaction centres immobilized on titanium dioxide. Photosynth Res 138(1):103–114

Brettel K (1997) Electron transfer in photosystem I. Biochim Biophys Acta 1318:322–373

Brettel K, Leibl W (2001) Electron transfer in photosystem I. Biochim Biophys Acta 1507:100–114

Carbonera D, Agostini G, Morosinotto T, Bassi R (2005) Quenching of chlorophyll triplet states by carotenoids in reconstituted Lhca4 subunit of peripheral light-harvesting complex of photosystem I. Biochemistry 44:8337–8346

Ciesielski PN, Scott AM, Faulkner CJ, Berron BJ, Cliffel JGK (2008) Functionalized nanoporous gold leaf electrode films for the immobilization of photosystem I. ACS Nano 2(12):2465–2472

Ciesielski PN, Hijazi FM, Scott AM, Faulkner CJ, Beard L, Emmet K, Rosenthal SJ, Cliffel D, Jennings GK (2010a) Photosystem I—based biohybrid photoelectrochemical cells. Bioresour Technol 101:3047–3053

Ciesielski PN, Faulkner CJ, Irwin MT, Gregory JM, Tolk NH, Cliffel DE, Jennings GK (2010b) Enhanced photocurrent production by photosystem I multilayer assemblies. Adv Funct Mater 20:4048–4054

Elli AF, Jelezko F, Tietz C, Studier H, Brecht M, Bittl R, Wrachtrup J (2006) Red pool chlorophylls of photosystem I of the

Cyanobacterium *Thermosynechococcus elongatus*: a single-molecule study. Biochemistry 45:1454–1458

Fairclough WV, Forsyth A, Evans MCW, Rigby SEJ, Purton S, Heathcote P (2003) Bidirectional electron transfer in photosystem I: electron transfer on the PsaA side is not essential for phototrophic growth in Chlamydomonas. Biochim Biophys Acta 1606:43–55

Feifel SC, Stieger KR, Lokstein H, Lux H, Lisdat F (2015) High photocurrent generation by photosystem I on artificial interfaces composed of π-system-modified graphene. J Mater Chem A 3:12188–12196

Fromme P, Grotjohan I (2008) Structure of photosystems I and II. Results Probl Cell Differ 45:33–72

Gibasiewicz K, Ramesh VM, Melkozernov AN, Lin S, Woodbury NW, Blankenship RE, Webber AN (2001) Excitation dynamics in the core antenna of PS I from *Chlamydomonas reinhardtii* CC 2696 at room temperature. J Phys Chem 105:11498–11506

Giera W, Gibasiewicz K, Ramesh VM, Lin S, Webber A (2009) Electron transfer from A0− to A1 in Photosystem I from *Chlamydomonas reinhardtii* occurs in both the A and B branch with 25–30-ps lifetime. Phys Chem Chem Phys 11:5186–5191

Giera W, Ramesh VM, Webber AN, van Stokkum IHM, van Grondelle R, Gibasiewicz K (2010) Effect of the P700 pre-oxidation and point mutations near A_0 on the reversibility of the primary charge separation in photosystem I from *Chlamydomonas reinhardtii*. Biochim Biophys Acta 1797:106–112

Giera W, Szewczyk S, McConnel MD, Snellenburg J, Redding KE, van Grondelle R, Gibasiewicz K (2014) Excitation dynamics in photosystem I from *Chlamydomonas reinhardtii*. Comparative studies of isolated complexes and whole cells. Biochim Biophys Acta 1837:1756–1768

Gizzie EA, Niezgoda JS, Robinson MT, Harris AG, Jennings KG, Rosenthal SJ, Cliffel DE (2015) Photosystem I-polyaniline/TiO_2 solid-state solar cells: simple devices for biohybrid solar energy conversion. Energy Environ Sci 8:3571–3576

Gobets B, van Stokkum IHM, Rogner M, Kruip J, Schlodder E, Karapetyan NV, Dekker JP, van Grondelle R (2001) Time-resolved fluorescence emission measurements of photosystem I particles of various cyanobacteria: a unified compartmental model. Biophys J 81:407–424

Gobets B, van Stokkum IHM, van Mourik F, Dekker JP, van Grondelle R (2003) Excitation wavelength dependence of the fluorescence kinetics in photosystem I particles from *Synechocystis* sp. PCC 6803 and *Synechococcus elongatus*. Biophys J 85:3883–3898

Gordiichuk PI, Wetzelaer GJAH, Rimmerman D, Gruszka A, De Vries JW, Saller M, Gautier DA, Catarci S, Pesce D, Richter S, Blom PW, Hermann A (2014) Solid-state biophotovoltaic cells containing photosystem I. Adv Mater 26:4863–4869

Guergova-Kuras M, Boudreaux B, Joliot A, Joliot P, Redding K (2001) Evidence for two active branches for electron transfer in photosystem I. Proc Natl Acad Sci USA 98:4437–4442

Gunther D, LeBlanc G, Prasai D, Zhang JR, Cliffel DE, Bolotin KL, Jennings GK (2013) Photosystem I on graphene as a highly transparent, photoactive electrode. Langmuir 29:4177–4180

Holzwarth AR, Muller MG, Niklas J, Lubitz W (2005) Charge Recombination fluorescence in photosystem I reaction centers from *Chlamydomonas reinhardtii*. J Phys Chem B 109:5903–5911

Holzwarth AR, Muller MG, Niklas J, Lubitz W (2006) Ultrafast transient absorption studies on photosystem I reaction centers from *Chlamydomonas reinhardtii*. 2: Mutations near the P700 reaction center chlorophylls provide new insight into the nature of the primary electron donor. Biophys J 90:552–565

Ito S, Chen P, Comte P, Nazeeruddin P, Liska MK, Pechy P, Gratzel M (2007) Fabrication of screen-printing pastes from TiO_2 powders for dye-sensitised solar cells. Prog Photovolt Res Appl 15(7):603–612

Jensen PE, Bassi R, Boekema EJ, Dekker JP, Jansson S, Leister D, Robinson C, Scheller HV (2007) Structure, function and regulation of plant photosystem I. Biochim Biophys Acta 1767:335–352

Joliot P, Joliot A (1999) In vivo analysis of the electron transfer within photosystem I: are the two phylloquinones involved? Biochemistry 38:11130–11136

Jordan P, Fromme P, Witt HT, Klukas O, Saenger W, Krauss N (2001) Three-dimensional structure of cyanobacterial photosystem I at 2.5A resolution. Nature 411:909–917

Karapetyan NV, Schlodder E, van Grondelle R, Dekker JP (2006) Advances in photosynthesis and respiration. In: Golbeck J (ed) Photosystem I the light-driven plastocyanin:ferredoxin oxidoreductase, vol 24. Springer, Netherlands, pp 177–192

Kurashov V, Gorka M, Milanovsky GE, Johnson TW, Cherepanov DA, Semanov AYu, Golbeck JH (2018) Critical evaluation of electron transfer kinetics in P700–FA/FB, P700–FX, and P700–A1 photosystem I core complexes in liquid and in trehalose glass. Biochim Biophys Acta Bioenerg 1859:1288–1301

Le Quiniou C, Tian L, Drop B, Wientjes E, van Stokkum IHM, van Oort B, Croce R (2015) PSI-LHCI of *Chlamydomonas reinhardtii*: increasing the absorption cross section without losing efficiency. Bichim Biophys Acta 1847:458–467

Li Y, van der Est A, Lucas MG, Ramesh VM, Gu F, Petrnko A, Lin S, Webber AN, Rappaport F, Redding K (2006) Directing electron transfer within photosystem I by breaking H-bonds in the cofactor branches. Proc Natl Acad Sci USA 103:2144–2149

Melkozernov AN, Kargul J, Lin S, Barber J, Blankenship RE (2004) Energy coupling in the PSI-LHCI supercomplex from the green alga *Chlamydomonas reinhardtii*. J Phys Chem B 108:10547–10555

Mershin A, Matsumoto K, Kaiser L, Yu D, Vaughn M, Nazeeruddin MK, Bruce BD, Graetzel M, Zhang S (2012) Self-assembled photosystem-I biophotovoltaics on nanostructured TiO_2 and ZnO. Sci Rep 2:234

Morosinotto T, Breton J, Bassi R, Croce R (2003) The nature of a chlorophyll ligand in Lhca proteins determines the far red fluorescence emission typical of photosystem I. J Biol Chem 278(49):49223–49229

Mukherjee D, Khomami B (2011) Photosystem I assembly on chemically tailored SAM/Au substrates for bio-hybrid device fabrication. Langmuir 26:16048–16054

Nelson N, Yocum CF (2006) Structure and function of photosystems I and II. Ann Rev Plant Biol 57:521–565

Ocakoglu K, Krupnik T, van den Bosch B, Harputlu E, Gullo MP, Olmos JDJ, Yildirimcan S, Gupta RK, Yakuphanoglu F, Barbieri A, Reek JNH, Kargul J (2014) Photosystem I-based biophotovoltaics on nanostructured hematite. Adv Funct Mater 24:7467

Ramesh VM, Gibasiewicz K, Lin S, Bingham SE, Webber AN (2004) Bierectional electron transfer in photosystem I: accumulation of A_0^- in A-side or B-side mutants of the axial ligand to chlorophyll A_0. Biochemistry 43:1369–1375

Ramesh VM, Gibasiewicz K, Lin S, Bingham SE, Webber AN (2007) Replacement of the methionine axial ligand to the primary electron acceptor A0 slows the A0- reoxidation dynamics in photosystem I. Biochim Biophys Acta 1767:151–160

Santabarbara S, Kuprov I, Fairclough WV, Purton S, Hore PJ, Heathcote P, Evans MCW (2005) Bidirectional electron transfer in photosystem I: determination of two distances between P700+ and A1- in spin-correlated radical pairs. Biochemistry 44:2119–2128

Santabarbara S, Kuprov I, Hore PJ, Casal A, Heathcote P, Evans MCW (2006) Analysis of the spin-polarized electron spin echo of the [P700+A1 -] radical pair of photosystem I indicates that both reaction center subunits are competent in electron transfer in cyanobacteria, green algae, and higher plants. Biochemistry 45:7389–7403

Savikhin S, Xu W, Soukoulis V, Chitnis PR, Struve WS (1999) Ultrafast primary processes in photosystem I of the *Cyanobacterium synechocystis* sp. PCC 6803. Biophys J 76(6):3278–3288

Shah VB, Henson WR, Chadha TS, Lakin G, Liu H, Blankenship RE, Biswas P (2015) Linker-free deposition and adhesion of photosystem I onto nanostructured TiO_2 for biohybrid photoelectrochemical cells. Langmuir 31(5):1675–1682

Slavov C, Ballottari M, Morosinotto T, Bassi R, Golzwarth AR (2008) Trap-limited charge separation kinetics in higher plant photosystem I complexes. Biophys J 94:3601–3612

Snellenburg JJ, Laptenok S, Seger R, Mullen KM, van Stokkum IHM (2012) Glotaran: a java-based graphical user interface for the R package TIMP. J Stat Softw 49:1–22

Stieger KR, Ciornii D, Kolsch A, Hejazi M, Lokstein H, Feifel SC, Zouni A, Lisdat F (2016a) Engineering of supramolecular photoactive protein architectures: the defined co-assembly of photosystem I and cytochrome *c* using a nanoscaled DNA-matrix. Nanoscale 8:10695–10705

Stieger KR, Feifel SC, Lokstein H, Hejazi M, Zouni A, Lisdat F (2016b) Biohybrid architectures for efficient light-to-current conversion based on photosystem I within scalable 3D mesoporous electrodes. J Mater Chem A 4:17009–17017

Szewczyk S, Giera W, D'Haene S, van Grondelle R, Gibasiewicz K (2017) Comparison of excitation energy transfer in cyanobacterial photosystem I in solution and immobilized on conducting glass. Photysnth Res 132(2):111–126

Szewczyk S, Giera W, Białek R, Burdziński G, Gibasiewicz K (2018) Acceleration of the excitation decay in photosystem I immobilized on glass surface. Photosynth Res 136(2):171–181

Szewczyk S, Abram A, Białek R, Haniewicz P, Karolczak J, Gapiński J, Kargul J, Gibasiewicz K (2020) On the nature of uncoupled chlorophylls in the extremophilic photosystem I-light harvesting I supercomplex. Biochim Biophys Acta 1861(2):148136

Trissl H-W (1993) Long-wavelength absorbing antenna pigments and heterogeneous absorption bands concentrate excitons and increase absorption cross section. Photosynth Res 35:247–263

van Amerongen H, Valkunas L, van Grondelle (2000) Photosynthetic excitons. World Scientific, Singapore, New Jersey, London, Hong Kong

Vassiliev IR, Jung YS, Mamedov MD, Semenov AYu, Golbeck JH (1997) Near-IR absorbance changes and electrogenic reactions in the microsecond-to-second time domain in photosystem I. Biophys J 72(1):301–315

Wientjes E, van Stokkum IHM, van Amerongen H, Croce R (2011) The role of the individual Lhcas in photosystem I excitation energy trapping. Biophys J 101:745–754

Woronowicz K, Ahmed S, Biradar A, Biradar A, Birnie V, Asefa D, Niederman T (2012) Near-IR absorbing solar cell sensitized with bacterial photosynthetic membranes. Photochem Photobiol 88(6):1467–1472

Yu D, Wang M, Zhu G, Ge B, Liu S, Huang F (2015) Enhanced photocurrent production by bio-dyes of photosynthetic macromolecules on designed TiO_2 film. Sci Rep 5:9375